JOURNAL OF CATALYSIS 147, 535–543 (1994)

Features of Li–Mn–MgO Catalysts and Their Relevance in the Oxidative Coupling of Methane

R. Mariscal, J. Soria, M. A. Peña, and J. L. G. Fierro[1]

Instituto de Catálisis y Petroleoquímica, CSIC, Campus UAM, Cantoblanco, 28049 Madrid, Spain

Received August 13, 1993; revised December 1, 1993

This work describes relevant structural features of the ternary Li–Mn–MgO system useful for the reaction of methane oxidative coupling. For a Mn–MgO catalyst, XRD, XPS, and ESR techniques revealed that manganese is incorporated into a Mg_6MnO_8 phase in which the formal oxidation state of manganese is Mn^{4+}. Addition of Li_2CO_3 in small amounts (0.48–1.60 wt.% Li) to the base Mn–MgO catalyst results in partial destruction of the Mg_6MnO_8 phase. TPR and XPS data showed that the reduction of manganese is easier in the bulk Mg_6MnO_8 compound than in the Mn–MgO catalyst and that it is inhibited by lithium. Moreover, the increase in Mn/Mg XPS intensity ratios in the lithium-doped counterparts indicates that lithium incorporation into the base Mn–MgO catalyst enhances manganese dispersion, in agreement with the increase of Mn^{4+}–Mn^{4+} distance derived from ESR spectra.

INTRODUCTION

Despite a decade of intense research activity on the oxidative coupling of methane (OCM), there is still much to be learned concerning the reaction and catalyst systems. Although a large variety of bulk and supported metal oxides have been found to be useful for the production of ethane and ethylene via OCM, little is known about the nature of surface sites responsible for the activation of methane. There now seems to be a general agreement that the principal role of the catalyst is the activation of the C–H bond of CH_4 giving a $CH_3\cdot$ radical which can desorb into the gas phase and combine with another radical to yield ethane (1).

In the pioneering work by Keller and Bhasin (2) on the screening of a number of reducible metal oxides for OCM, it was found that manganese oxide displays the best performance when operating in a cyclic feed of air and methane. The amount of oxygen transferred to the catalysts and then to the methane was many times larger than that which could have been adsorbed on the catalyst surface, indicating that oxygen must have diffused into and out of the bulk of the catalyst to at least 10–20 atomic layer below the surface. Increased yields of higher hydrocarbons from CH_4 over Mn-based catalysts have already been achieved upon addition of alkali metals and alkaline earths to the base catalysts (3–5). This improvement arises largely by suppression of the formation of carbon oxides. For a somewhat more complex system such as $NaMnO_4/MgO$, Labinger *et al.* (6) postulated that the active component could be the Mg_6MnO_8 phase, which exhibits a high ionic mobility. Contrary to the above findings, Hinsen *et al.* (7) studied the OCM reaction over a series of reducible oxides, including those of Sn, Pb, Mn, and Bi, but by cofeeding the reactants, and found that MnO_x oxides catalyze the combustion of methane with only a very low proportion of C_2 hydrocarbons formed. A careful study by Chan and Smith (8) over manganese and magnesium oxide systems emphasized the importance of solid-state reactions to form the active phases.

The intrinsic limitation of high ion mobility in redox type catalysts is absent in alkaline and alkaline earth oxides which have shown quite good catalytic performance for the OCM reaction (9–14). Without doubt, among this latter category, lithium-doped magnesium oxide catalyst, first reported by Lunsford's group (15, 16) and then confirmed by others (17–19), is one of the most efficient catalysts. The disadvantage of the Li/MgO system is that the highest C_2 selectivities and yields are reached at relatively high temperatures (above 1023 K). Under these severe conditions, lithium is lost (20, 21), either through reaction with the reactor wall or by formation of volatile LiOH.

In line with the above arguments, it appears tempting to incorporate both manganese and lithium into a MgO carrier in order to exploit the beneficial effect of Mn on catalyst stability and CH_4 conversion and of lithium on C_2 hydrocarbon selectivity. Although there are a few recent reports related to the behaviour of the ternary system Li–Mn–MgO (22–25) in the OCM reaction, only little is known about the nature of phases, or the structure of the solid close to the surface. The work of Cimino *et al.* (26, 27) and of Cordischi *et al.* (28, 29) demonstrated that manganese ions can be incorporated into MgO in different

To whom correspondence should be addressed.

0021-9517/94 $6.00

phases or as solid solutions. In the current investigation, several techniques, including TPR, XRD, XPS, and ESR, have been used to monitor both surface and bulk properties of Li–Mn–MgO catalysts with different lithium contents in an effort to determine their relevance on the OCM reaction.

EXPERIMENTAL

Catalyst Preparation

Magnesium oxide (99.6%) powder obtained from U.C.B. (Brussels) was used as carrier. Prior to impregnation with Mn and/or Li salts, it was calcined in air at 1073 K for 4 h. A manganese-containing catalyst was prepared by adding MgO to an aqueous solution of manganese nitrate ($Mn(NO_3)_2 \cdot 4H_2O$, Riedel-de Haën AG) in the appropriate concentration and evaporating to dryness. The precursor was kept at ambient temperature for 16 h, then dried at 403 K for 10 h and subsequently calcined in air at 1073 K for 4 h. This catalyst will be referred to as Mn–MgO. The same experimental procedure was repeated for the preparation of the Mg_6MnO_8 compound whose stoichiometric composition represents 16.7 wt.% Mn. An aliquot of the Mn/MgO catalyst was then impregnated with an aqueous solution of Li_2CO_3 (Merck, reagent grade). In order to increase the solubility of Li_2CO_3, CO_2 was bubbled into the solution and the flask was maintained under ice. Once solutions become transparent, the required amount of Mn/MgO was added to the flask solution and then the excess water was removed. Drying and calcination steps were the same as given above. The two lithium-doped catalysts, containing 0.48 and 1.60 wt.% Li, will be referred to hereafter as 1Li–Mn–MgO and 2Li–Mn–MgO, respectively. A summary of the samples and their compositions determined by atomic absorption spectrometry are compiled in Table 1.

Experimental Techniques

X-ray diffraction patterns were recorded using a Philips PW 1010 vertical diffractometer using nickel-filtered Cu$K\alpha$ radiation, under constant instrumental parameters. For each sample, Bragg angles between 5 and 70° were scanned at a rate of 2°/min.

Temperature-programmed reduction (TPR) experiments were carried out in a Cahn 2000 microbalance working at a sensitivity of 10 μg. The samples were heated in a flow of helium (99.995% vol) (60 ml/min) to 923 K in order to remove adsorbed water and other gaseous contaminants. They were cooled to 423 K in the same flow of helium; this was then switched to hydrogen (99.994% vol) (60 ml/min) and the samples were again heated at a rate of 4 K/min while continuously recording the weight changes. The microbalance was interfaced to a data station which allowed accumulation and processing of the results of weight change vs temperature.

X-ray photoelectron spectra were acquired with a Fisons ESCALAB MkII 200R spectrometer equipped with a hemispherical electron analyzer and a Mg$K\alpha$ X-ray exciting source (1253.6 eV, 1 eV = 1.6022×10^{-19} J). The samples were mounted on a sample rod placed in a pretreatment chamber and heated under vacuum or in hydrogen at 773 K for 1 h prior to being moved into the analysis chamber. The pressure in the ion-pumped analysis chamber was below 3×10^{-9} Torr (1 Torr = 133.3 N m^{-2}) during data acquisition. Twenty eV energy regions of the photoelectrons of interest were scanned at a 20 eV spectrometer pass energy, chosen as a compromise enabling acceptable resolution to be obtained within reasonable data acquisition time. C 1*s*, O 1*s*, Mn 2*p*, Mg 2*p* and Li 1*s* peaks were recorded. The intensities were estimated by calculating the integral of each peak after subtraction of the S-shaped background and fitting the experimental curve to a mixture of Lorentzian and Gaussian lines of variable proportion (30). All binding energies (BE) were referenced to the adventitious C 1*s* line at 284.9 eV. This reference gave BE values accurate to within ±0.2 eV.

The ESR spectra were obtained with a Bruker ER 200 D spectrometer operating in the X-band. A modulation of 100 kHz and a dpph standard with $g = 2.0036$ were used. The powdered samples (50 mg) were placed within a vacuum quartz cell assembled with greaseless stopcocks capable of maintaining a vacuum better than 2.3×10^{-5} Torr. Spectra of the catalysts were recorded at 77 K after treatments either in vacuum at 773 K for 1 h or after reduction by H_2 under 100 Torr at 773 K for 1 h.

TABLE 1

Nomenclature and Chemical Analysis of Manganese-Containing Catalysts

Sample	%Mn[a]	%Li[b]	[Li]/[Mn][c]
Mg_6MnO_8	14.15	—	—
Mn–MgO	5.53	—	—
1Li–Mn–MgO	5.72	0.48	0.66
2Li–Mn–MgO	5.73	1.60	2.21

[a] Expressed as Mn atom.
[b] Expressed as Li atom.
[c] Atomic ratio.

RESULTS

The X-ray diffraction (XRD) patterns of the Mn–MgO catalyst and its lithium-doped 1Li–Mn–MgO and 2Li–Mn–MgO homologues are compiled in Fig. 1. For comparative purpose, the XRD patterns of the reference compounds MgO and Mg_6MnO_8 are also included in Fig. 1. Comparison of the XRD patterns of these two reference

compounds shows the appearance of the most intense lines at very close diffraction angles. The differentiation has been possible by recording at very low speed the expanded region of diffraction angles 60–65°, in which the (200) and (440) reflections for MgO and Mg6MnO$_8$ are positioned at 62.2 and 62.7°, respectively. The XRD pattern of the Mn–MgO catalyst (Fig. 1c) when compared with that of the reference compound MgO (Fig. 1a) and Mg_6MnO_8 (Fig. 1b) shows the presence of a mixture of MgO and Mg_6MnO_8 phases. The same situation is observed for the two Li-doped counterparts, although a decrease in the specific diffraction lines of the Mg_6MnO_8 phase is observed, particularly clearly for the 2Li–Mn–MgO sample. The intensity of the lines of the MgO phase remains essentially unchanged. These findings suggest that lithium incorporation into the base Mn–MgO catalyst results in a strong modification of the Mg_6MnO_8 phase, probably because lithium could be incorporated into a new manganese-containing phase, as previously found for similar catalysts (22). It is emphasized that if this latter interpretation applies, such a new Li–Mn phase must be highly dispersed or even amorphous, as no new diffraction lines were detected.

Integral weight changes as a function of the reduction temperature for the manganese-containing catalysts are summarized in Fig. 2. The two lithium-free Mg_6MnO_8 (Fig. 2, curve b) and Mn–MgO (Fig. 2, curve c) catalysts

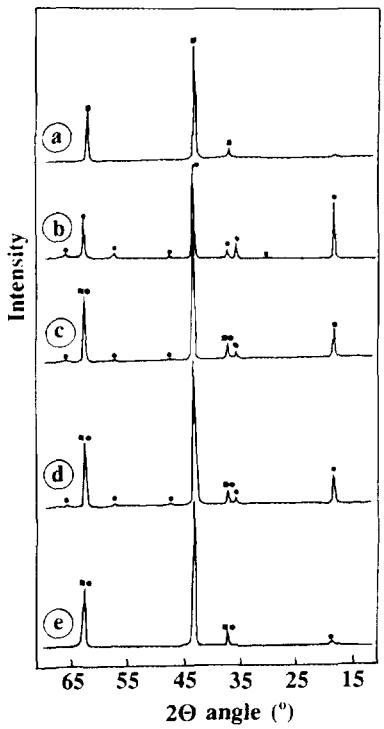

FIG. 1. X-ray diffraction patterns of manganese-containing catalysts and of reference compounds: (a) MgO, (b) Mg_6MnO_8, (c) Mn–MgO, (d) 1Li–Mn–MgO, and (e) 2Li–Mn–MgO.

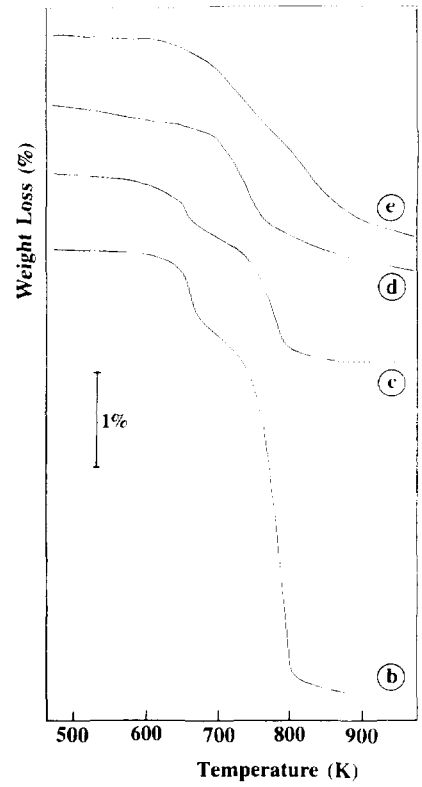

FIG. 2. Integral weight changes (%) as a function of the temperature of reduction of manganese-containing catalysts: (b) Mg_6MnO_8, (c) Mn–MgO, (d) 1Li–Mn–MgO, and (e) 2Li–Mn–MgO. As the ordinate is common for all catalysts, a bar corresponding to 1% weight loss has been inserted in this Figure. Curve tables facilitate comparison with other figures.

display two well-resolved reduction steps, the high-temperature step being much larger for the former. These profiles change markedly for the two lithium-containing catalysts. The 1Li–Mn–MgO (Fig. 2, curve d) shows a single reduction step, while two poorly resolved steps can be discerned for the parent 2Li–Mn–MgO (Fig. 2, curve e) catalyst. In order to define more accurately the temperatures at which the maximum weight changes occur, the integral data were differentiated. These derivative curves are displayed in Fig. 3 and the temperatures of the maxima of the peaks are compiled in Table 2. Three peaks can be distinguished for Mg_6MnO_8 and Mn–MgO catalysts: there is one well-resolved low-temperature peak at 668 K and two other overlapping peaks located at temperatures above 770 K. The intensity of the low-temperature peak is substantially lower than that of the high-temperature peak. These TPR profiles were dramatically changed upon incorporation of lithium into the Mn–MgO base catalyst. For the 1Li–Mn–MgO catalyst (Fig. 3, curve d) a single asymmetric peak at 741 K with a long tail extending to the lower temperature side is observed, whereas two broader peaks placed at ca. 723 and 823 K (Fig. 3, curve e) can be discerned for its 2Li–Mn–MgO homologue. These results

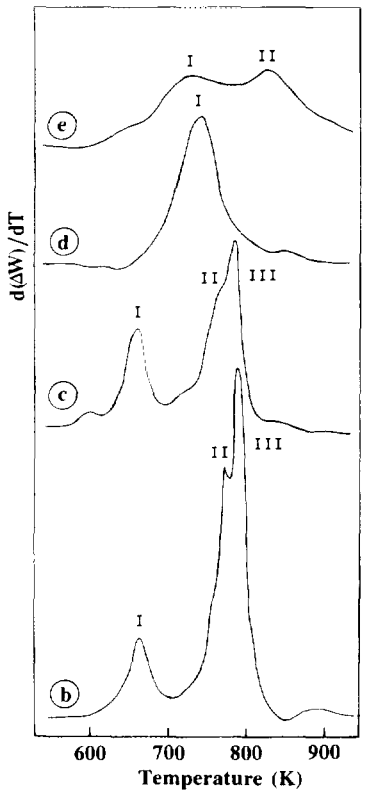

FIG. 3. Derivative curves of the temperature-programmed reduction profiles presented in Fig. 2 for all manganese-containing catalysts. The notation is the same as in Fig. 2.

compare rather well with TPR data of Bradshaw *et al.* (31) and Baronetti et al. (13) on K-doping in MnO_2-based catalysts, which showed a broad doublet at 673–773 K on the TPR profile of pure MnO_2 and also the reduction of this doublet and its shift to higher temperatures (973–1073 K) upon addition of KCl to the MnO_2 catalyst.

TABLE 2

Position of Peaks and Weight Changes Derived from TPR Profiles

Catalyst	Peak	T_{max} (K)	Exp. weight loss (%)	Theor. weight loss (%)
Mg_6MnO_8	I	668	4.83	4.12
	II	773		
	III	786		
Mn–MgO	I	668	2.03	1.61
	II	773		
	III	786		
1Li–Mn–MgO	I	741	1.93	1.61
2Li–Mn–MgO	I	723	2.32	1.61
	II	823		

TABLE 3

Binding Energies (eV) of Core Electrons and XPS Intensity Ratios

Sample	Pretre.	C 1*s*	O 1*s*	Mn $2p_{3/2}$	Mg 2*p*	Li 1*s*	I_{Mn}/I_{Mg}
Mg_6MnO_8	Va. 673 K	284.9	529.8	642.6	49.4	—	0.877
MnMgo	Va. 673 K	284.9	530.4	642.5	49.8	—	0.252
		289.8	531.4				
1Li–Mn–MgO	Va. 673 K	284.9	530.0	642.5	49.4	54.6	0.469
		289.3	531.7				
2Li–Mn–MgO	Va. 673 K	284.9	529.5	642.5	49.1	54.6	0.501
		289.7	531.6		51.0		
Mg_6MnO_8	H_2, 773 K	284.9	529.5	640.5	47.1	—	0.834
		288.8	531.4	642.3	49.1		
MnMgO	H_2, 773 K	284.9	529.6	639.6	48.3	—	0.297
		288.7	531.7	641.5	49.2		
1Li–Mn–MgO	H_2, 773 K	284.9	529.5	641.3	48.8	54.1	0.444
		288.9	531.6				
2Li–Mn–MgO	H_2, 773 K	284.9	529.4	641.7	48.8	54.7	0.661
		289.5	531.5				

Table 2 also summarizes the experimental weight losses for all the Mn-containing catalysts and the expected theoretical losses for complete reduction of Mn^{4+} to Mn^{2+}. It can be seen that the experimental weight losses are slightly higher than the theoretical ones assuming complete reduction of Mn^{4+} to Mn^{2+}. By comparing the high BE C 1*s* XPS peaks of calcined and H_2-reduced catalysts in Figs. 4A and 4B, respectively, this finding can be interpreted in terms of CO_2 removal produced from the decomposition of surface carbonates under hydrogen treatment.

XP spectra for all calcined and H_2-reduced manganese-containing catalysts were recorded. Prior to XPS analysis, calcined samples were heated at 773 K under vacuum in the pretreatment chamber of the spectrometer to remove adsorbed water and to decompose the $Mg(OH)_2$ formed by adsorption of moisture. The binding energies of the most intense peaks in the XP spectra are summarized in Table 3 for each calcined and H_2-reduced sample. Figure 4A displays C 1*s* spectra from calcined samples. These samples revealed a large hydrocarbon or amorphous carbon peak at 284.9 eV (32) and a second carbonate peak in the range 289.3–289.8 eV, which probably resulted from CO_2 adsorption (11, 14, 33). Comparison of the BE values of the carbonate peak of the two lithium-free samples (spectra b and c) with those of the lithium-doped samples (spectra d and e) does not allow us to distinguish between carbonates associated with magnesium or lithium. As can be seen below, this assignment is only feasible after H_2-treatment at 773 K. Figure 4A shows also that the intensity of the carbonate peak is even higher than that of the contamination peak for the Mn–MgO catalyst but decreases upon lithium incorporation, more noticeably for high Li content. However, the lowest carbonate peak is found for the Mg_6MnO_8 catalyst. Interestingly, there is an opposite trend between the intensity of the carbonate peaks and the exposure of manganese ions.

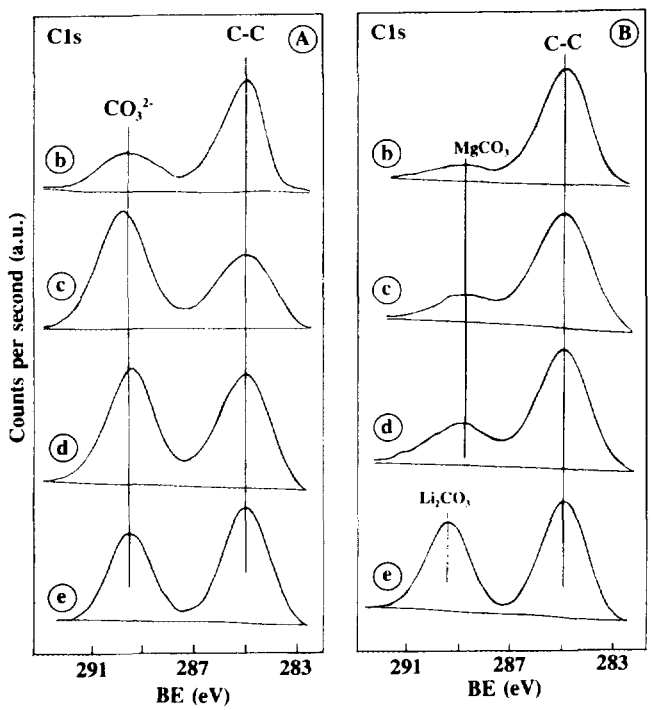

FIG. 4. C 1*s* core level spectra of manganese-containing catalysts: (b) Mg_6MnO_8, (c) Mn–MgO, (d) 1Li–Mn–MgO, and (e) 2Li–MgO. The samples were first outgassed at 773 K for 1 h and then reduced in hydrogen at 773 K for 1 h. (A) Calcined and (B) H_2-reduced catalysts.

The H_2-reduced catalysts also display the two C 1*s* peaks, although substantial changes in both BE and intensities of the carbonate peak are observed (Fig. 4B). With the exception of the 2Li–Mn–MgO catalyst (spectrum e), which shows both BE and intensity of the carbonate essentially the same as its calcined homologue, the Mg_6MnO_8 (spectrum b), Mn–MgO (spectrum c), and 1Li–Mn–MgO (spectrum d) catalysts display the carbonate peak at ca. 288.8 eV and decrease in intensity with respect to the parent calcined catalysts. In agreement with literature observations which showed by using X-ray powder diffraction (34), thermogravimetric analysis (17), and XPS (33) that Li_2CO_3 appears as the stable phase on Li–MgO catalyst under OCM conditions, these results suggest that Li_2CO_3 is the dominant carbonate species in the 2Li–Mn–MgO and probably in the 1Li–Mn–MgO catalyst. The other carbonate peak (ca. 288.8 eV) still remaining in the H_2-pretreated catalysts could be due associated with Mg^{2+} cations. Considering the strong decrease of its intensity when the Li-free catalysts are pretreated in hydrogen for 1 h, it is inferred that its concentration would be even decreased upon prolonged pretreatments under the same conditions.

The O 1*s* peaks are much less conclusive for carbonate assignment. As shown in Table 3, all O 1*s* spectra of calcined catalysts display two peaks: there is one at ca. 529.5 eV due to lattice O^{2-} species from MgO and/or Mg_6MnO_8 species and another at ca. 531.5 eV due to $MgCO_3$ and Li_2CO_3. As the BE of the latter peak does not change with H_2 treatment, differentation between these carbonates is not possible from the O 1*s* profile alone. The BE values for the Mn $2p_{3/2}$ peaks in both calcined and reduced samples are also given in Table 3. For the calcined samples, values at ca. 642.5 eV are consistent with the BEs of Mn^{4+} species (35). The situation is more complex for the H_2-reducted catalysts. As can be seen in Fig. 5, the Mn $2p_{3/2}$ peak shows, after peak deconvolution, at least two components. A peak at ca. 640.5–640.6 eV is observed together with that at ca. 642.5 eV, with the exception of the 2Li–Mn–MgO catalyst which shows only one peak at 641.7 eV. It should be emphasized at this point that for all the Mn $2p_{3/2}$ spectra the fit included a broad component towards the high BE side for peak area measurements: the origin of this component is physical in nature, being due to energy relaxation and final state effects. From the position of the Mn $2p_{3/2}$ peaks on the BE scale it is clear that the peak at ca. 642.5 eV is assigned to Mn^{4+} species, while the lower BE peak is due to Mn^{2+} (36); the peak at 641.7 eV can therefore be assigned to Mn^{3+} species. It can also be noted in Fig. 5 that the relative proportion of reduced Mn species is higher in the reduced

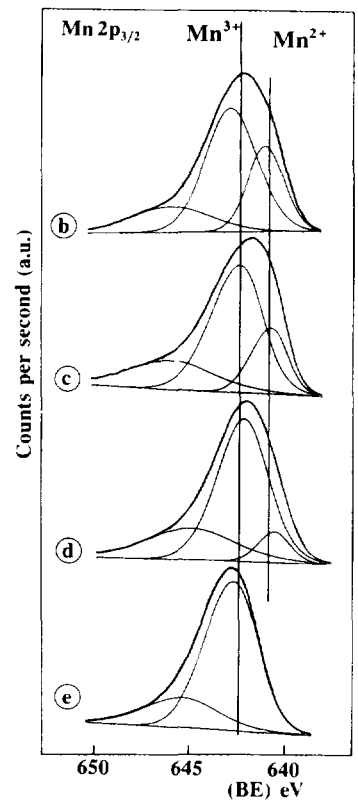

FIG. 5. Mn 2*p* core level spectra of manganese-containing catalysts: (b) Mg_6MnO_8, (c) Mn–MgO, (d) 1Li–Mn–MgO, and (e), 2Li–Mn–MgO. The samples were first outgassed at 773 K for 1 h and then reduced in hydrogen at 773 K for 1 h.

Mg_6MnO_8 compound than in the Mn–MgO catalyst, and smaller in its 1Li–Mn–MgO counterpart, disappearing in the 2Li–Mn–MgO catalyst. All of these facts suggest that the reduction of manganese is easier in the bulk Mg_6MnO_8 than in the Mn–MgO catalysts and that it is inhibited by lithium.

The Mn 2*p* intensities relative to that of magnesium (I_{Mn}/I_{Mg}) for calcined and reduced catalysts may be compared from data listed in Table 3. The very high value of this ratio for the Mg_6MnO_8 sample suggests a high degree of dispersion for manganese at the surface. Judging from this ratio, the lowest value for the Mn–MgO catalyst indicates poor dispersion of manganese; however, lithium incorporation into the base Mn–MgO catalyst enhances the manganese dispersion. Finally, no significant changes in these ratios are observed between calcined and H_2-reduced catalysts.

The ESR spectra of manganese-containing samples outgassed at 295 K are displayed in Fig. 6A and the characteristic ESR parameters are summarized in Table 4. The spectra of the two lithium-free samples Mg_6MnO_8 (Fig. 6A, spectrum b) and Mn–MgO (Fig. 6A, spectrum c) show a symmetric signal with g = 1.9953 (signal A) and

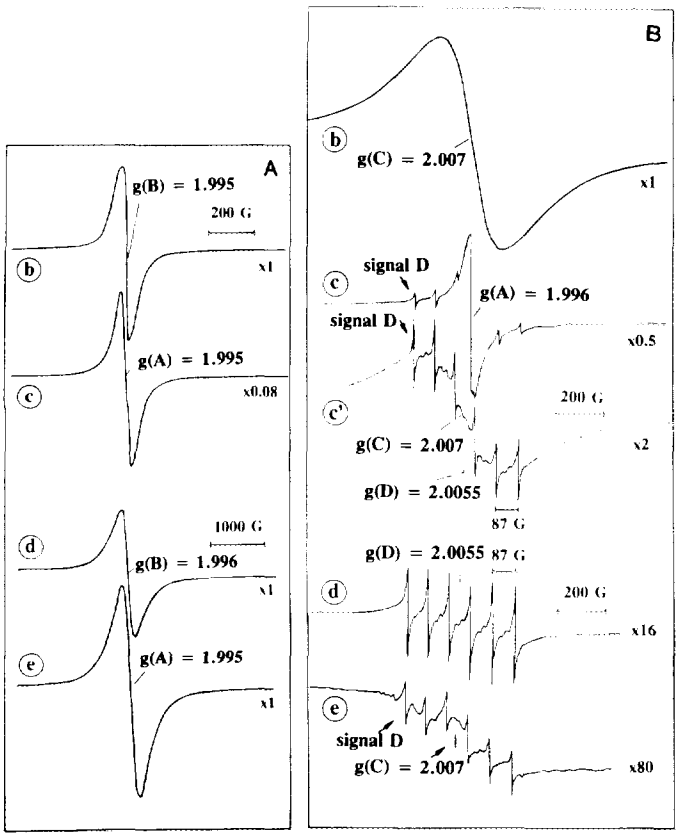

FIG. 6. ESR spectra of manganese-containing catalysts subjected either to outgassing at room temperature (A) or to reduction in hydrogen at 773 K for 1 h (B): (b) Mg_6MnO_8, (c) Mn–MgO, (c') the same as (c) but reduced at 973 K, (d) 1Li–Mn–MgO, and (e), 2Li–Mn–MgO.

TABLE 4

ESR Parameters and Assignments of Manganese Signals

Signal	g	ΔH_{pp} (G)	hfs (G)	Assignment
A	1.995	43	—	Exchange interacting Mn^{4+}
B	1.996	>300	—	Dipolar interacting Mn^{4+}
C	2.007	310	—	Dipolar interacting Mn^{2+}
D	2.0055	8.4	87	Isolated Mn^{2+}

ΔH_{pp} = 43 G. As the nuclear spin of Mn is I = 5/2, a hyperfine structure of six lines would be expected if the paramagnetic manganese ions are located at magnetically isolated positions. However, the absence of hyperfine structure, the narrow linewidth, and the g value below 2 indicate that the manganese centers responsible for such a signal are Mn^{4+} ions (29, 37), strongly interacting (exchange interactions) with their neighbours. In the case of Mg_6MnO_8, with an average distance between manganese ions of 0.59 nm, this type of interaction is to be expected. The situation is somewhat different for the two lithium-containing catalysts. Although their spectra show symmetric signals with g values below 2, indicating that they are due to Mn^{4+} ions, the ΔH_{pp} values markedly increased to 310 G for catalyst 1Li–Mn–MgO (Fig. 6A, spectrum d) and to 340 G for catalyst 2Li–Mn–MgO (Fig. 6A, spectrum e), signal type B. This indicates that the magnetic interactions, although still important, are of different types (dipolar interactions) due to an increase of the distance between the Mn^{4+} ions. Signals due to solid solution of manganese in MgO are not observed, probably because considering the low solubility of manganese their signal should be very much smaller than the Mn^{4+} signal.

The changes in ESR signals brought about by reduction in hydrogen at 773 K are illustrated in Fig. 6B. The Mg_6MnO_8 catalyst, prereduced at 773 K (Fig. 6B, spectrum b), displays a symmetric ESR signal with a g value somewhat above 2 (signal C), typical of Mn^{2+} ions and ΔH_{pp} = 310 G, without hyperfine splitting, indicating that these ions are affected by dipolar interactions. This finding suggests that compared to the manganese reduction, the Mn–Mn interactions are weaker than in the calcined sample, indicating that the average distance between manganese ions has increased. For the sample of Mn–MgO reduced at 773 K for 1 h, the appearance of signal A and a smaller signal with resolved hfs (signal D with g = 2.0055, a = 87 G) due to Mn^{2+} ions probably in solid solution in MgO (Fig. 6B, spectrum c) can be taken as indicative that the reduction of this catalyst, under the experimental conditions used for ESR measurements, is more difficult than in the parent Mg_6MnO_8 bulk compound. The difficulty of reducing Mn^{4+} ions in the Mn–MgO catalyst is also consistent with its ESR spectrum when treated in H_2 at 973 K (Fig. 6B, spectra c'),

which shows the elimination of signal A (Mn^{4+} ions), the increase of signal D, and the formation of signal C due to Mn^{2+} ions. For the two lithium-containing catalysts (Fig. 6B, spectra d and e) signal D is observed, although much less intense, indicating a lower incorporation of Mn into MgO, and overlapping with a broad signal B in the 2Li–Mn–MgO catalyst. The low intensity in these two spectra could indicate a certain stabilization of the ESR-silent Mn^{3+} ions, which depends on the lithium content.

DISCUSSION

Catalyst Structures

The solid state reaction between manganese oxide and the MgO substrate during the calcination step at 1073 K led to the formation of Mg_6MnO_8 when manganese and magnesium were present at the stoichiometric ratio. This result indicates that the manganese cations were introduced as Mn^{4+} ions and formed a compound maintaining this oxidation state. The incorporation of manganese to magnesium oxide as Mn^{2+} ions is not favoured under our experimental conditions, although Cordischi and Lo Jacono (28) have found Mn^{2+} in MgO after calcination at 1273 K. The XRD pattern of the Mn–MgO catalyst (Fig. 1) revealed the presence of two crystalline phases, namely MgO and Mg_6MnO_8, in a ratio (calculated using the lines at *d*-spacings of 0.210 and 0.485 nm) of 3. This result and those obtained by XPS (Fig. 5 and Table 3) and by ESR (Fig. 6A, spectrum c), for which the parameters of the ESR signal are essentially the same as that of the Mg_6MnO_8 compound, indicate that again in this sample the manganese cations remain as Mn^{4+}. Further support for the presence of Mn^{4+} ions in calcined catalyst is provided not only by the high BE of the Mn $2p_{3/2}$ peak but also by the slightly higher experimental weight loss (2.03%) of the catalyst upon reduction by hydrogen and the theoretical value (1.61%) expected for complete reduction of Mn^{4+} to Mn^{2+} (cf. Table 2).

Lithium incorporation into the base Mn–MgO catalyst leads to significant structural modifications. As observed in the XRD patterns of the lithium-containing catalysts (Figs. 1d and 1e), the intensity of the peaks due to the Mg_6MnO_8 phase decreased to a great extent upon the second impregnation of the Mn–MgO precursor with a Li_2CO_3 solution. The XRD pattern of sample 1Li–Mn–MgO indicates that the Mg_6MnO_8/MgO ratio has dropped slightly and for sample 2Li–Mn–MgO the Mg_6MnO_8 contribution has practically disappeared. These ternary *x*Li–Mn–MgO systems still retain a fraction of Li_2CO_3, and more specifically the 2Li–Mn–MgO catalyst, as confirmed by the presence of a strong C 1*s* XPS peak at 288.9 eV (Fig. 4, spectrum e). Accordingly, lithium seems to interact easily with manganese and, as indicated by the marked linewidth increase of the ESR Mn^{4+} signal, lead to an increase of the distance between Mn^{4+} cations. This manganese modification will be reflected in the Mg_6MnO_8 crystallinity.

Two types of interaction must be considered to explain the changes in ESR linewidths. At intermediate Mn–Mn distances, the dipolar interactions are strong enough to increase the linewidths, preventing the observation of the hyperfine structure due to the nuclear spin of manganese. If the Mn ions are placed at shorter distances (0.59 nm), the exchange interactions can be important and consequently a narrow single signal would be observed. While the latter situation can be identified with the formation of Mg_6MnO_8, the increase of the distance between isolated Mn^{4+} ions could be produced by the reduction to Mn^{3+} of some cations in Mg_6MnO_8, or more likely to the formation of some amorphous lithium–manganese mixed oxide. In agreement with XPS data, spectra d and e in Fig. 6A confirm that manganese becomes more and more dispersed upon incorporation of lithium into the base Mn–MgO catalyst. On the basis of these two sets of experiments it is suggested that most of the lithium is incorporated into a Li–Mn–O phase. However, if the proportion of manganese is higher than that required for the stoichiometry of the mixed oxide, the excess Mn^{4+} ions can still form Mg_6MnO_8, which for 1Li–Mn–MgO can still be present.

It has been reported that lithium and manganese form a crystalline Li_2MnO_3 phase (23, 25) detectable by XRD. For the catalysts presented here, the formation of a crystalline tridimensional Li_2MnO_3 phase is only favourable for the 2Li–Mn–MgO catalyst, whose Li/Mn = 2.21 (Table 1) is still higher than the stoichiometry Li/Mn = 2 of this compound. Apart from this consideration, it is clear that the XPS Mn/Mg intensity ratio increases markedly when lithium is added to the base Mn–MgO catalyst (Table 3, last column), indicating that lithium enhances the manganese dispersion.

One could speculate about the possibility of lithium forming an interaction with the MgO substrate, but no new crystalline phases were detected by XRD. The presence of an amorphous or very finely divided Li–Mg–O phase can, in principle, be discarded, as only a single photoelectron Mg 2*p* peak was observed.

Reduced Species

The reaction conditions for the OCM reaction are clearly different from those used for the TPR sequence. The reductions identified by TPR are unlikely to occur, as presented here, under methane coupling conditions, especially when complete consumption of oxygen does not occur. Despite this limitation, a comparison of the TPR profiles for the Mn–MgO catalyst and the model

Mg_6MnO_8 compound, and for the Mn–MgO and its lithium-doped counterparts, is very useful. As already discussed above, the XRD, XPS, and ESR data lead to the conclusion that Mn^{4+} was the only manganese species present in calcined catalysts. However, the reduction profiles of these Mn^{4+} species are strongly altered by the presence of lithium. The ESR spectra for the Li-containing samples showed an easier reduction of the Mn^{4+} ions than for the Li-free counterparts.

Reduction by hydrogen (static) at 773 K led to marked differences. While most of the manganese is reduced to Mn^{2+} in the Mg_6MnO_8 sample, the reduction is less uniform for sample Mn–MgO, containing both MgO and Mg_6MnO_8 phases, as Fig. 6B, spectrum c shows both Mn^{4+} and Mn^{2+} ions. In this latter case, the marked intensity decrease with respect to its outgassed homologue (Fig. 6A, spectrum c) indicates the formation of ESR-silent species such as diamagnetic manganese coupled pairs or, more likely, Mn^{3+} ions. The observation of the ESR signal of Mn^{2+} ions in MgO indicates that when the manganese ions are reduced to Mn^{2+}, their incorporation into the MgO lattice is much easier. Still considering the differences in the reduction conditions in ESR and TPR experiments, a careful inspection of the TPR profiles of the two samples in Fig. 3, although they look similar, reveals a more uniform reduction of sample Mg_6MnO_8, probably because of an interaction with the existing MgO. The Li-containing catalysts show a different situation after H_2 reduction. The absence of ESR signals due to Mn^{4+} ions and the presence of weak signals due to Mn^{2+} ions isolated in MgO and interacting magnetically in some reduced oxide can be interpreted as resulting from stabilization of most of the manganese as Mn^{3+} in the presence of lithium, as indicated by the XPS results and explaining the peak at 740 K in the TPR curves. The effect of stabilization of Mn^{3+} ions is even more marked for the 2Li–Mn–MgO catalyst. For this sample the formation of a different mixed oxide could justify the TPR peak at 850 K and the lower incorporation of Li to MgO indicated by ESR in Fig. 6B, spectrum e.

The close similarity between TPR profiles for Mg_6MnO_8 and Mn–MgO catalysts (Fig. 3, curves b and c, respectively) can be taken as conclusive that manganese is present in the same phase, thereby supporting the XPS and ESR data. The low-temperature TPR peak can be associated with the reduction of Mn^{4+} to Mn^{3+} on the Mg_6MnO_8 surface, while the high-temperature peaks can be reasonably assigned to the reduction of Mn^{3+} to Mn^{2+} (22). Moreover, by assuming that the area of peak I is substantially lower than that of peak III, peak II might be associated with a small proportion of the remaining unreduced Mn^{4+}. In favour of this interpretation is the reduction of the Mg_6MnO_8 compound in a CH_4 flow, instead in hydrogen, which showed a single and broad peak positioned at the temperature of peak III. When comparing these results with the Mn $2p_{3/2}$ core level spectra of the reduced catalysts (Fig. 5) it is clear that the extent of formation of reduced Mn species is very sensitive to the experimental conditions of the reduction. As the samples for XPS experiments were reduced at 773 K, this temperature is somewhat below that of peak III in TPR profiles, explaining the appearance of a small proportion of reduced manganese (Mn^{3+} and/or Mn^{2+}) in the Mn $2p_{3/2}$ peaks of Fig. 5. Finally, it is important to emphasize that irrespective of this limitation, lithium incorporation inhibits the reduction of manganese. As a consequence, lower oxygen mobilities in the complex Li–Mn–MgO catalyst systems would limit carbon oxide formation in favour of dimerization products.

CONCLUSION

Manganese reaction with MgO at 1073 K in air leads to the formation of a Mg_6MnO_8 phase in which the formal oxidation state of manganese is Mn^{4+}, as confirmed by TPR, XPS, and ESR techniques. Important modifications in catalyst structure occur when lithium is added to the base Mn–MgO catalyst. XPS and ESR reveal that manganese becomes more dispersed upon the incorporation of lithium, suggesting formation of a Li–Mn–O phase. Although Cordischi and LoJacono (28) have found Mn^{2+} in MgO after calcination at 1273 K, incorporation of manganese to magnesium oxide as Mn^{2+} ions is not favoured under our experimental conditions. Reduction by hydrogen led to marked differences. At 773 K most of these manganese in Mg_6MnO_8 is reduced to Mn^{2+}, while this reduction is not so important in Mn–MgO catalyst. For the lithium-containing samples, the absence of an ESR signal due to Mn^{4+} ions and the presence of weak signals due to Mn^{2+} ions point to the stabilization of Mn^{3+} ions. The inhibition of the reduction of manganese upon Li incorporation is also confirmed by XPS data.

ACKNOWLEDGMENTS

This research was supported by the Comisión Interministerial de Ciencia y Tecnología, Spain (Grants MAT88-0239 and MAT91-0494). The authors also acknowledge Dr. J. A. Anderson for critical reading of the manuscript.

REFERENCES

1. Ekstrom, A., and Lapszewicz, J. A., *J. Am. Chem. Soc.* **110,** 5226 (1988).
2. Keller, G. E., and Bhasin, M. M., *J. Catal.* **73,** 9 (1982).
3. Sofranko, J. A., Leonard, J. J., and Jones, C. A., *J. Catal.* **103,** 302 (1987); U.S. Patents 4,443,644; 4,443,645; 4,443,646; 4,443,647; 4,443,648; 4,443,649; and 4,444,984 to Atlantic Richfield Co. (1984).
4. Jones, C. A., Leonard, J. J., and Sofranko, J. A., *J. Catal.* **103,** 311 (1987).

5. Sofranko, J. A., Leonard, J. J., Jones, C. A., Gaffney, A. M., and Withers, H. P., *Catal. Today* **3,** 127 (1988).
6. Labinger, J. A., Ott, K. C., Mehta, S., Rockstad, H. K., and Zoumalan, S., *J. Chem. Soc., Chem. Commun.*, 543 (1987).
7. Hinsen, W., Bytyn, W., and Baerns, M., *in* "Proceedings, 8th International Congress on Catalysis, Berlin, 1984," Vol. 3, p. 581. Dechema, Frankfurt-am-Main, 1984.
8. Chan, T. K., and Smith, K. L., *Appl. Catal.* **60,** 13 (1990).
9. Burch, R., Squire, G. D., and Tsang, S. C., *Appl. Catal.* **43,** 105 (1988).
10. Burch, R., Chalker, S., Squire, G. D., and Tsang, S. C., *J. Chem. Soc., Faraday Trans. 1* **86,** 1607 (1990).
11. Grzybek, T., and Baerns, M., *J. Catal.* **129,** 106 (1991).
12. Peng, X. D., and Stair, P. C., *J. Catal.* **128,** 264 (1991).
13. Baronetti, G. T., Scelza, O. A., Castro, A. A., Cortés Corberán, V., and Fierro, J. L. G., *Appl. Catal.* **61,** 311 (1990).
14. Baronetti, G. T., Padró, C., Scelza, O. A., Castro, A. A., Cortés Corberán, V., and Fierro, J. L. G., *Appl. Catal.* **101,** 167 (1993).
15. Driscoll, D. J., and Lunsford, J. H., *J. Phys. Chem.* **89,** 4415 (1985).
16. Ito, T., and Lunsford, J. H., *Nature* **314,** 721 (1985).
17. Kimble, J. B., and Kolts, J. H., *CHEMTECH* **17,** 501 (1987).
18. Hutchings, G. J., Scurrell, M. S., and Woodhouse, J., *J. Chem. Soc., Chem. Commun.*, 1862 (1987).
19. Roos, J. A., Bakker, A. G., Bosch, H., van Ommen, J. G., and Ross, J. R. H., *Catal. Today* **1,** 133 (1987).
20. Korf, S. J., Roos, J. A., de Bruijn, N. A., van Ommem, J. G., and Ross, J. R. H., *J. Chem. Soc., Chem. Commun.*, 1433 (1987).
21. Korf, S. J., Roos, J. A., Bruijn, N. A., van Ommem, J. G., and Ross, J. R. H., *Catal. Today* **2,**535 (1988).
22. Larkins, F. P., and Nordin, M. R., *J. Catal.* **130,** 147 (1991).
23. Larkins, F. P., and Nordin, M. R., *in* "Methane Conversion" (D. B. Bibby, C. D. Chang, R. F. Howe, and S. Yurchak, Eds.), Vol. 36, p. 409. Elsevier, Amsterdam, 1988.
24. Korf, S. J., Roos, J. A., Veltman, L. J., van Ommen, J. G., and Ross, J. R. H., *Appl. Catal.* **56,** 119 (1989).
25. Choudhary, V. R., Rajput, A. M., Akolekar, D. B., and Seleznev, V. A., *Appl. Catal.* **62,** 171 (1990).
26. Cimino, A., Lo Jacono, M., Porta, P., and Valigi, M., *Z. Phys. Chem.* **59,** 134 (1968).
27. Cimino, A., and Indovina, V., *J. Catal.* **17,** 54 (1970).
28. Cordischi, D., and Lo Jacono, M., *Z. Phys. Chem.* **74,** 93 (1974).
29. Cordischi, D., Nelson, R. L., and Tench, A. J., *Trans. Faraday Soc.* **65,** 2740 (1969).
30. Shirley, D. A., *Phys. Rev.* **35,** 4909 (1972).
31. Bradshaw, D. I., Coolen, P. T., Judd, R. W., and Komodromos, C., *Catal. Today* **6,** 427 (1990).
32. See, for instance, "Practical Surface Analysis. Auger and X-ray Photoelectron Spectroscopy, 2nd Edition" (D. Briggs and M. P. Seah, Eds.), Wiley, New York, 1990.
33. Peng, S. D., Richards, D. A., and Stair, P. C., *J. Catal.* **121,** 99 (1990).
34. Ito, T., Wang, J. X., Lin, C. H., and Lunsford, J. H., *J. Am. Chem. Soc.* **107,** 5062 (1985).
35. Ivanov-Emin, B. N., Nevskaya, N. A., Zaitsev, B. E., and Ivanova, T. M., *Zh. Neorg. Khim.* **27,** 3101 (1982).
36. Oku, M., Hirokawa, K., and Ikeda, S., *J. Electron Spectrosc. Relat. Phenom.* **7,** 465 (1975).
37. Henderson, B., and Hall, T. P. P., *Proc. Phys. Soc., London* **90,** 511 (1967).